RSC Advances

PAPER

View Article Online
View Journal | View Issue

Cite this: *RSC Adv.*, 2024, **14**, 1612

Calcium ferrites for phosphate adsorption and recovery from wastewater†

Matheus Henrique Pimentel Araújo, *[a] José Domingos Ardisson, [b] Alisson Carlos Krohling, [b] Rochel Montero Lago, [c] Walber Guimarães Júnior [d] and Juliana Cristina Tristão [a]

Received 28th August 2023
Accepted 19th December 2023

DOI: 10.1039/d3ra05871a

rsc.li/rsc-advances

In this study, calcium ferrites with different Ca : Fe atomic ratios (1 : 1, 1 : 2, 1 : 3 and 2 : 1) were prepared from Ca and Fe nitrates treated at 300, 700 and 900 °C and evaluated for phosphate adsorption and recovery from wastewater. TG, XRD, Mössbauer spectroscopy, SEM, VSM magnetic measurements, and BET analyses showed the formation of two different calcium ferrite phases, *i.e.*, $CaFe_2O_4$ and $Ca_2Fe_2O_5$ at 700 and 900 °C. The adsorption results indicated that the formation of calcium ferrite structure is critical for phosphate adsorption/recovery. Evaluation of the pH, initial phosphate concentration, contact time, coexisting ions and desorption conditions showed remarkable adsorption capacities of 62–75 mg g^{-1} for CaFe1:2-700 and 28–43 mg g^{-1} for CaFe1:2-900. The phosphate adsorption on the Ca ferrite surfaces is so strong that the recovery/desorption showed limited efficiencies, *e.g.*, 15–39%.

Introduction

Given the problems associated with phosphate pollution of lakes, rivers and oceans and the decreasing availability of phosphate rock in the coming years, several alternatives have been developed for water treatment and recovery of phosphate and other nutrients.[1–7] These include chemical precipitation, biological treatment, constructed wetlands, electrodialysis, reverse osmosis, nanofiltration and adsorption.[1,4]

Adsorption processes have several advantages when phosphate concentrations in water are low, such as simplicity, cost, no sludge formation, and the possibility of adsorbent regeneration.[1,4] Several compounds have been tested for phosphate adsorption, *e.g.*, zeolites,[8] activated carbon and biochar,[1] metal-doped mesoporous silica, mesoporous metal oxide, mesoporous carbon,[9] and carbonate materials.[1]

In recent years, ferrous materials have been used for phosphate adsorption, such as hematite (Fe_2O_3), goethite (FeOOH), magnetite (Fe_3O_4), and other magnetic nano-adsorbents. Ajmal *et al.*[10] studied the phosphate adsorption in ferrihydrite, goethite and magnetite and observed adsorption capacities of *ca.* 16, 15, and 13 mg g^{-1}, respectively. Liu *et al.*[11] used ferrihydrite (Fh), goethite (Gt) and hematite (Hm) to evaluate the removal of Cd^{2+} and PO_4^{3-} in water. The minerals showed a decreasing behavior Fh (28.4 mg g^{-1}) > Gt (9.7 mg g^{-1}) > Hm (4.7 mg g^{-1}) for phosphate removal. Zinc ferrite nanoparticles were used for phosphate adsorption and showed low phosphate removal capacity at an initial concentration of 5 mg L^{-1}.[12]

Materials containing alkaline earth metals (Ca, Mg) have been used for phosphate removal.[13,14] In the work of Han *et al.*,[15] calcium and magnesium ferrites were synthesized by the combustion method using PVA and applied for phosphate removal. The results showed that calcium and magnesium iron oxides could increase the phosphate removal capacity of the material. The samples without PVA showed better results, Fe/$CaCl_2$-NoPVA and Fe/$MgCl_2$-NoPVA with *ca.* 17 mg g^{-1}. However, the presence of PVA resulted in a lower adsorption capacity for these materials due to the nanoparticle coating. Jia *et al.*[16] used a layered double hydroxide containing Ca with 182.5 mg g^{-1} for phosphate removal. A CaMg-based layered double hydroxide was used in real effluent from a wastewater treatment plant and removed >90% of phosphate.[17] Mg–Al and Zn–Al layered double hydroxides effectively removed over 90% of phosphate from aqueous solution.[18] Cheng *et al.*[19] prepared a cost-effective anhydrite-BPM sorbent (ABPM) by mixing anhydrite and brucite-periclase materials with phosphate removal of 23.6 mg g^{-1}. Calcium aluminate decahydrate was used to achieve low phosphate concentrations. In a column experiment, Sonoda *et al.*[20] used granular ferric oxides for phosphate adsorption and

[a]*Universidade Federal de Viçosa – Campus Florestal – UFV, Rodovia LMG 818, km 06, s/n, Campus Universitário, Florestal, MG, 35690-000, Brazil. E-mail: matheus.pimentel@ufv.br*

[b]*Centro de Desenvolvimento da Tecnologia Nuclear – CDTN/CNEN, campus da Universidade Federal de Minas Gerais, Avenida Presidente Antônio Carlos, No 6627, Rua Mário Werneck, S/N – Pampulha, Belo Horizonte, MG, Brazil*

[c]*Universidade Federal de Minas Gerais – UFMG, Avenida Presidente Antônio Carlos, No 6627, Rua Mário Werneck, 2 – Pampulha, Belo Horizonte, MG, 31270-901, Brazil*

[d]*Universidade Federal de São Carlos – UFSCar, Rodovia Washington Luís, s/n – Monjolinho, São Carlos – SP, 13565-905, Brazil*

† Electronic supplementary information (ESI) available. See DOI: https://doi.org/10.1039/d3ra05871a

showed that alkaline earth metal ions significantly increased phosphate adsorption.

Reusability and lifespan are essential factors to consider when evaluating the potential use of adsorbents in water treatment. Adsorbents that have a longer useful life and excellent recyclability allow for a reduction in the operational cost of the adsorption process.[21,22] There are two ways in the literature for regeneration and reuse of the adsorbent: extraction of the adsorbed phosphate through desorption and restoration of the original structure of the adsorbent. In the recovery of phosphate adsorbents, different solutions containing NaOH and $NaHCO_3$/Na_2CO_3 at different concentrations can extract the adsorbed phosphate through desorption.[21–25] Regeneration is generally carried out through alkaline washing (pH > 13), where P accumulates and is later recovered. Aggressive chemicals can deteriorate the adsorbent, reducing its performance and useful life. After regeneration, the regenerated adsorbent may differ from the fresh adsorbent; incomplete desorption of phosphate is also possible.[4,21,22,24,25]

This work prepared calcium ferrite adsorbents by a simple route synthesis at different Ca : Fe (1 : 1, 1 : 2, 1 : 3, 2 : 1) atomic ratios and calcination temperatures (300, 700 and 900 °C). Different techniques characterized the materials and provided insights into the structure and composition of the adsorbents. The material was applied for phosphate adsorption and recovery in different conditions to evaluate the phosphate adsorption capacity of calcium ferrites. This information provided insights into the proposal of an adsorption mechanism. Calcium ferrite's phosphate desorption capacity was also evaluated under different conditions to elucidate the better desorption condition.

Methods

Calcium ferrites synthesis

The samples were synthesized by the thermal decomposition method without organic precursors. The $Ca(NO_3)_2 \cdot 4H_2O$ (ÊXODO CIENTÍFICA) and $Fe(NO_3)_2 \cdot 9H_2O$ (NEON) reagents were used as analytical standards and different Ca : Fe molar ratios (1 : 1; 1 : 2; 1 : 3 and 2 : 1) measured (SHIMADZU ATY224). The mass of different proportions was solubilized with 50 mL of deionized water (GEHAKA) and kept under magnetic stirring at 90 °C until dry (IKA). The dried samples were calcined in the tube furnace (Sanchis 1200) at different temperatures of 300, 700 and 900 °C for one hour with a heating rate of 5 °C min^{-1}. The materials were crushed after calcination using mortar and pestle. The material identification is presented in the ESI Table S1.†

Materials characterization

Different techniques characterized the materials. Thermal analysis TG/DTA studied the thermal stability of the materials. The analyses were performed on a Shimadzu TG/DTA (model DTG-60H) in the air atmosphere with a gas flow of 50 mL min^{-1} and a heating rate of 10 °C min^{-1}, ranging from 25° to 900 °C. X-ray diffraction (XRD) was used to identify the crystalline phases. The materials were characterized by XRD using SHIMADZU (XRD-7000 X-ray diffractometer, Cu Kα radiation), voltage 30.0 kV, current 30.0 mA and continuous scanning range from 4.0 to 70.0° 2θ. The diffractograms were analyzed in Profex software for phase identification according to the Crystallography Open Database.[26] The transmission ^{57}Fe Mössbauer measurements were obtained at 293 K, with a ^{57}Co/Rh source. The Normos least-squares fits were used to calculate the spectral hyperfine parameters, and the isomeric deviations (IS) were standardized concerning natural Fe (α-Fe). The morphology of the materials was observed using a Scanning Electron Microscope (SEM) using a Quanta 200 FEG instrument. Energy dispersive spectroscopy (EDS) was performed on a carbon plate with the same instrument at 5 keV. The surface area was determined by N_2 absorption using the BET method in an Autosorb 1 Quantachrome instrument and the data were analyzed in ASiQwin (5.21) software. The magnetic properties of the samples were measured using a vibrating sample magnetometer (VSM, Lakeshore model 7404) at room temperature. The magnetic hysteresis curve was obtained up to a magnetic field of 1.8 Tesla (18 kOe).

Adsorption study

Phosphate adsorption experiments. Phosphate adsorption was measured with batch adsorption experiments, which allowed the measurement of the adsorption capacity of the samples and the more efficient sample for the following experiments. The experiment used 20 mg of material and 20 mL of phosphate solution at 100 mg L^{-1} KH_2PO_4 (Vetec) in conical propylene flasks and was performed in triplicate. The flasks were stirred at 200 rpm for 24 h at room temperature (ETHINK). The samples were centrifuged at 3900 rpm (FANEM) for 15 min and filtered through a 0.22 μm syringe filter (KASVI). The ascorbic acid method described in standard methods for the examination of water and wastewater determined the phosphate adsorption capacity. The preliminary test was performed on samples before and after washing.

Effect of pH and point of zero charge (pH_{PZC}) on adsorption. To investigate the influence of pH on the phosphate adsorption, 20 mg of adsorbent was kept in contact with 20 mL of phosphate solution (100 mg L^{-1}) for 24 hours at 200 rpm, at room temperature. The pH of the solution was adjusted with HCl (0.1 mol L^{-1}) or NaOH (0.1 mol L^{-1}) and measured by pH tape (Macherey-Nagel). The phosphate concentration was determined by the ascorbic acid method.

In determination of the point of zero charge (PZC), the experiment was performed by an adapted 11 points method proposed by de Freitas *et al.*[27]

Adsorption selectivity – effect of coexisting anions. The competition experiments were conducted with anions commonly present in wastewater to evaluate the influence of coexisting anions. Sulfate (SO_4^{2-}), nitrate (NO_3^-), chloride (Cl^-), carbonate (CO_3^{2-}) and bicarbonate (HCO_3^-) anions were selected because they are more abundant in wastewater. Then, 20 mg of adsorbent was kept in contact with 20 mL of different phosphate/ion solutions at the same concentration (100 mg L^{-1}) for 24 hours, 200 rpm, at room temperature.

Adsorption isotherms. Phosphate adsorption isotherms were determined using bath tests. The experiments were performed with 20 mg of adsorbents and 20 mL of phosphate solution with different concentrations of 25, 50, 100, 150, 200, 250, and 300 mg L^{-1} at conical propylene flasks. The flasks were kept in the incubator for 24 hours at 25 °C under 200 rpm. Then, the phosphate concentration was determined in the same way as previously described. The data obtained were analyzed according to the Langmuir, Freundlich[12] and Temkin mathematical models for two parameters isotherms and Redlich–Peterson (R–P) for tree parameters isotherm model.

Adsorption kinetics. Adsorption kinetics experiments were performed with 100 mL of phosphate solution at 100 mg L^{-1} and kept in contact with 100 mg of adsorbent in the erlenmeyer glass flask at 200 rpm and 25 °C. Aliquots were taken at different times: 0, 10, 20, 30, 60, 120, 180, 240, 300, 360, 420, 480, 720, 1440, 2160 and 2880 min, 1 mL. The samples were centrifuged for 5 min at 3900 rpm (ETHIK) and filtered through a 0.22 μm syringe filter (KASVI). The phosphate concentration was determined as previously described. The data obtained were analyzed by pseudo-first order and pseudo-second order as described by Gu *et al.*[12]

Desorption tests. The desorption tests were conducted to evaluate the recovery and reuse of materials in phosphate removal. Three conditions were applied: alkaline solutions, different ionic strengths, and a citric acid extractor. Many studies describe using alkaline solutions for phosphate recovery,[10,12] using different concentrations of NaOH. Therefore, at room temperature, 20 mg of adsorbent was kept in contact with 20 mL of NaOH in different concentrations of 0.1, 0.5, and 1 mol L^{-1} solution for 24 hours, 200 rpm. In addition, other ionic strength solutions can be used for desorption to simulate a soil condition. Desorption experiments were performed using different ionic strengths; 20 mg of adsorbent was kept in contact with 20 mL KCl at 1 mol L^{-1} and 0.2 mol L^{-1}, steering at 200 rpm for 24 hours at room temperature. The desorbed phosphate concentrations were determined by the ascorbic acid method. The Ministério da Agricultura, Pecuária and Abastecimento (MAPA) from Brazil describe other methods for characterizing phosphorus soluble in 2% citric acid to solid fertilizers. In the MAPA method, 150 mg of adsorbent and 20 mL of 2% citric acid solution were stirred at 40 rpm for 30 min. The phosphate concentration was then determined by the molybdovanadophosphoric acid spectrophotometric method.

Theoretical studies

Models. The bulk $Ca_2Fe_2O_5$ (Fig. 1a) and $CaFe_2O_4$ (Fig. 1b) contain 36 atoms ($Z = 4$) and 28 atoms ($Z = 4$), respectively. Each crystal structure belongs to the space group *Pnma* (no. 62). The lattice constants of the $Ca_2Fe_2O_5$ are $a = 5.381$ Å, $b = 14.613$ Å, and $c = 5.591$ Å.[28] There are 8 Fe ions in each cell. The 4 Fe ions are surrounded by tetrahedral oxygen coordination, and the other 4 Fe ions are surrounded by octahedral oxygen coordination. FeO_4 tetrahedra shares the corner oxide ion with FeO_6 octahedra. $Ca_2Fe_2O_5$ consists of FeO_6 octahedral and FeO_4 tetrahedral layers alternating along the *b*-axis, while the tetrahedral layer consists of tetrahedral chains along the *a*-axis. The chiral alternation of the tetrahedral chains between layers gives the centrosymmetric structure. The Ca ion is located between the FeO_4 tetrahedral and FeO_6 octahedral layers. The $CaFe_2O_4$ structure, Fig. 1b, consists of an edge- and corner-shared FeO_6 octahedral network, in which the lattice parameters are $a = 9.218$ Å, $b = 3.017$ Å and $c = 10.693$ Å.[29,30]

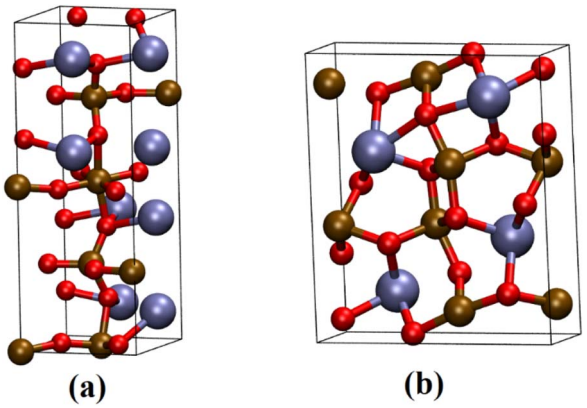

Fig. 1 Representation of the (a) $Ca_2Fe_2O_5$ and (b) $CaFe_2O_4$ unit cell. The brown, red, and blue spheres represent Fe, O, and Ca atoms.

Methods. Structural relaxations and self-consistent field calculations are performed with the PWscf code based on density functional theory (DFT)/plane waves and pseudopotentials with the Quantum ESPRESSO (QE)[31] code suite. The generalized gradient approximation (GGA) for the exchange–correlation function due to the revised Perdew–Burke–Ernzerhof model (RPBE)[32] was used within the interaction of valence electrons with nuclei and core electrons framework, which were treated by the Projector Augmented-Wave (PAW)[33] method. These were expanded in a plane wave basis set, and the cutoff energy was optimized for each system to ensure a total energy convergence within 1.0 meV. The structures were optimized when the convergence threshold for total energy and force for ionic minimization was set in the 10^{-6} and 10^{-5}, respectively. The convergence threshold for self-consistency was set to 10^{-10} a.u. Kinetic energy cutoffs of 80 Ry (1.09 keV) and 480 Ry (6.53 keV) were chosen to describe the wave function and the charge density, respectively. Integrations over the Brillouin zone were performed using a $4 \times 2 \times 4$ and $2 \times 8 \times 2$ Monkhorst–Pack *k*-point mesh for $Ca_2Fe_2O_5$ and $CaFe_2O_4$ systems, respectively, for the self-consistent field (SCF). Spin-polarized DFT + *U* calculations were performed, and the systems were initialized using antiferromagnetic ground state spin orderings with a Fe-sextet multiplicity $\left(s = \frac{5}{2}\right)$.[29,34,35] In this study, the effective Hubbard parameter (U_{eff}) was included following the DFT + *U* calculations were performed within the rotationally invariant formulation by Dudarev *et al.*[36] by applying an anisotropic Hubbard correction[37,38] to Fe-3d states with self-consistent *U* values computed *via* DFPT.[39] Hubbard parameters were computed by perturbing all inequivalent Fe-sites. The parameters were set at $U(\mathrm{Fe}_{\mathrm{O}_h}^{\mathrm{CaFe_2O_4}}) = 4.06$ eV for all $\mathrm{Fe}^{\uparrow}$-sites and

$U(Fe_{O_h}^{CaFe_2O_4}) = 3.84$ for all $Fe^{\downarrow}$-sites in the $CaFe_2O_4$ structure and $U(Fe_{O_h}^{Ca_2Fe_2O_5}) = 4.06$ eV for all Fe-octahedral atoms and $U(Fe_{T_d}^{Ca_2Fe_2O_5}) = 4.32$ eV for all Fe-tetrahedral atoms for the $Ca_2Fe_2O_5$ structure. The Mössbauer calculation was carried out in the QE-GIPAW routine,[40] which allows the calculation of relevant parameters and provides the opportunity to clarify many important structural details. The cutoff energy was set as 120 Ry (1.63 keV), and the kinetic energy cutoff was set as 600 Ry (8.16 keV) for charge density and potential. The electron–ion interactions were described with the Gauge-Including Projector Augmented Wave (GIPAW) pseudopotentials, which allowed the calculation of the Mössbauer-based quantities. The self-consistent criterion was the total energy difference between the two subsequent calculations being less than 10–15 Ry. We then investigate possible correlations of the predicted quadrupole splitting and isomer shift with local atomic geometry or local electronic structure, described by Bader analysis,[41,42] implemented in the CRITIC2 program,[43] and Born dynamical effective charges. The electronic density was generated by post-processing using the Mössbauer calculation protocol.

Results and discussions

In this study, calcium ferrites with different Ca : Fe atomic ratios (0 : 1, 1 : 1, 1 : 2, 1 : 3, 2 : 1) were prepared from the Ca and Fe nitrates by simple dissolution in water, drying and thermal treatment at 300, 700 and 900 °C. TG, XRD, Mössbauer, SEM, VSM and BET characterized the obtained solids.

Characterization of adsorbent materials

Thermogravimetric analysis. TGA was performed to determine the thermal stability of materials. Analyses in the air atmosphere obtained for CaFe1:2 precursors are shown in Fig. 2; the other samples are shown in ESI S1–S3.† Fig. 2 shows a sequence of weight loss up to 900 °C. The first step occurs below 100 °C and is likely related to dehydration processes (5.6%). From 100 to 200 °C, a second weight loss (15.3%) is probably associated with iron nitrate $Fe(NO_3)_3$ decomposition. A significant weight loss occurs between 350 and 500 °C (22.7%) and may be related to calcium nitrate $Ca(NO_3)_2$ decomposition. Similar weight losses have been described for similar materials.[44,45] There is a mass loss between 600 and 650 °C, 4.6%, but it is unclear what process is taking place. Late processes of dihydroxylation or nitrate decomposition may be related to this loss. In addition, more specific and detailed studies are needed to elucidate this process. Fig. 2 shows no weight loss after 700 °C. Calcium ferrites are typically formed at temperatures higher than 600 °C (ref. 46) or high pressures, as in the hydrothermal synthesis method.[47,48]

X-ray diffraction. All samples were characterized by X-ray diffraction to identify the crystalline phases and study the molar atomic ratio and temperature effect in the crystalline phase formation. Fig. 3 shows the XRD for CaFe1:2, CaFe1:2-300, CaFe1:2-700 and CaFe1:2-900, respectively.

The XRD patterns for samples CaFe1:2 and CaFe1:2-300 showed low crystallinity with diffraction peaks related to hematite (α-Fe_2O_3 – COD 04-003-2900). Note that the crystallinity of the material increased with temperature, as indicated by more intense and defined peaks observed in the patterns for samples CaFe1:2-700 and CaFe1:2-900. In addition, at higher annealing temperatures, 700 and 900 °C, the ferrite phases $CaFe_2O_4$ (COD 9013281) and $Ca_2Fe_2O_5$ (COD 9013469), both in the orthorhombic structure, are observed. It can be noted that the peak near 2θ 32.9°, referred to as hematite, suffers a dislocation to 2θ 33.4° after calcination at 700 °C, but refers to calcium ferrite phases, as shown in Fig. 3 by the dotted line. Other works show that high temperatures are necessary for forming $CaFe_2O_4$ formation.[46,49,50] The $CaFe_2O_4$ phase in the spinel structure has not been identified. The ionic diameter size of calcium Ca^{2+} makes the cation incorporation into the tetrahedral site complex for spinel structure formation, requiring higher temperatures or longer calcination time for its phase formation.[46,49,50] In the theoretical studies, the calculated lattice parameters of the orthorhombic unit cell for both structures are in satisfactory good agreement with the experimental values reported in the ESI (S11).†[28,30]

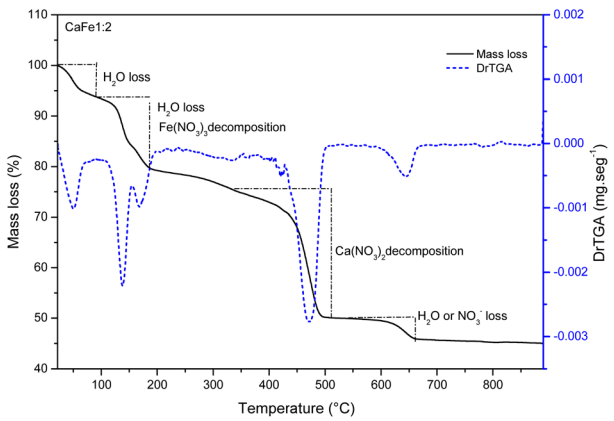

Fig. 2 Thermal decomposition curve and DTG for the sample CaFe1:2 at air atmosphere (50 mL min^{-1}) and heating rate of 10 °C min^{-1}.

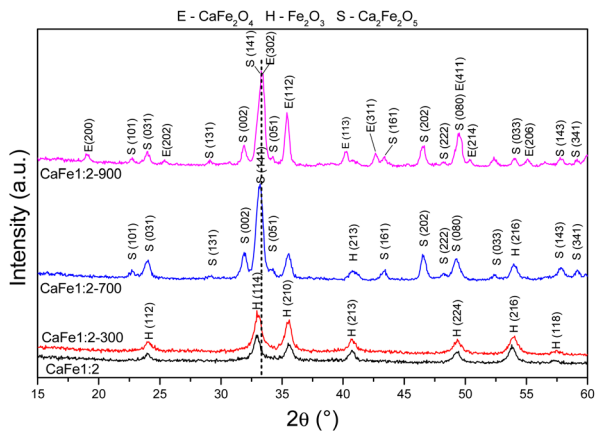

Fig. 3 Diffractograms of synthetic adsorbents prepared in the proportion Ca : Fe 1 : 2 calcined at different temperatures 300, 700 and 900 °C for one hour at a rate of 5 °C min^{-1}.

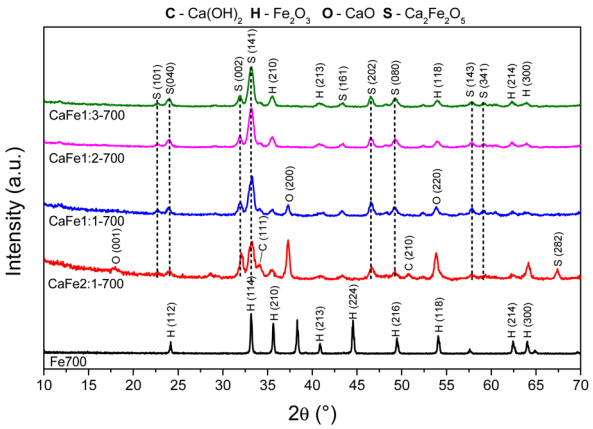

Fig. 4 Diffractograms of synthetic adsorbents prepared in the proportions Ca : Fe 1 : 1, 1 : 2, 1 : 3 and 2 : 1 calcined at 700 °C for one hour at a rate of 5 °C min^{-1}.

Fig. 4 and 5 show the Ca : Fe (0 : 1, 1 : 1; 1 : 2; 1 : 3, and 2 : 1) samples calcined at 700 and 900 °C for one hour, respectively, to analyze the effect of different atomic ratios. The Fe700 and Fe900 patterns show thin and intense peaks, indicating a material with high crystallinity. Both patterns indicate a phase formed from hematite (α-Fe_2O_3 – COD 04-003-2900). When calcium is present in the reaction mixture, the $2\theta = 33°$ peak is broadened. The patterns indicate different phases in this region (α-Fe_2O_3 – COD 04-003-2900), $CaFe_2O_4$ (COD 9013281) and $Ca_2Fe_2O_5$ (COD 90-134-69), which can cause peak enlargement. For samples with a higher iron content, CaFe1:2-700 and CaFe1:3-700, peaks related to hematite are still observed. In contrast to CaFe1:2-900 and CaFe2:1-900 samples, the ferrite phase $CaFe_2O_4$ (PDF 00-032-0168) is observed, and the hematite-related peaks become less prominent. Samples CaFe2:1 and CaFe2:1-300, in ESI S6,† present characteristic peaks for calcium nitrate ($Ca(NO_3)_2$) (COD 04-006-5679). This identification indicates an incomplete decomposition for this precursor, as discussed for TG analyses. The CaO (COD 04-007-9734) and $Ca(OH)_2$ (COD 04-010-3117) phases were identified for the Ca : Fe 2 : 1 and Ca : Fe 1 : 1 groups, which have the highest calcium molar ratio. The presence of $Ca(OH)_2$ may be related to the hydration of CaO with the water in the atmosphere during the sample storage. In the CaFe1:1-700, CaFe1:1-900, CaFe2:1-700, and CaFe2:1-900 samples, CaO (COD 04-007-9734), $hkl = (200)$, at 2θ near to 37° was identified. Excess Ca in these samples leads to the formation of impurities and may affect adsorption. It also indicates that not all the calcium available for the reaction is converted to the crystalline ferrite phase.

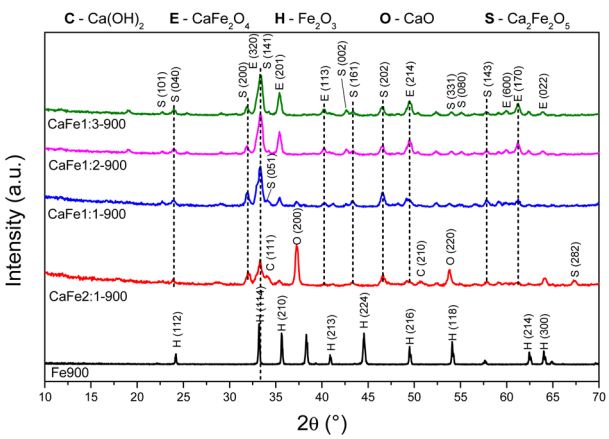

Fig. 5 Diffractograms of synthetic adsorbents prepared in the proportions Ca : Fe 1 : 1, 1 : 2, 1 : 3 and 2 : 1 calcined at 900 °C for one hour at a rate of 5 °C min^{-1}.

Table 1 shows the crystallite size calculated by the Scherrer equation. The crystallite size increases after 900 °C, indicating a more crystalline material formed at this temperature. The $Ca_2Fe_2O_5$ phase shows an increase of 30% in crystallite size from CaFe1:1-700 to CaFe1:1-900. The $Ca_2Fe_2O_5$ phase is preferentially formed for this Ca : Fe 1 : 1 ratio, as previously observed in the work of Hirabayashi *et al.*[50] The crystallite size increase with increasing calcination temperature is repeated for Ca : Fe ratios of 1 : 3 and 2 : 1.

For CaFe1:2-700 and CaFe1:2-900, the $Ca_2Fe_2O_5$ average crystallite size decreased by 16% after calcination at 900 °C for one hour. On the other hand, the $CaFe_2O_4$ phase was only observed for samples calcined at 900 °C for one hour, and the average crystallite size is larger than that of the $Ca_2Fe_2O_5$ phase. At this temperature, the $CaFe_2O_4$ phase predominates.[49–51] Many papers emphasize that the stoichiometric ratio and the calcination temperature are key factors in synthesizing a calcium ferrite monophase.[49,51] However, due to the variation in the Ca : Fe ratios and calcination time used in this work, two ferrite phases could be identified after treatment at 900 °C.

Mössbauer spectroscopy. The Mössbauer spectroscopy was performed to examine the valence state of iron and the type of coordination polyhedron occupied by iron atoms. Fig. 6 shows the Mössbauer spectra at room temperature for samples in Ca : Fe 1 : 2 ratio uncalcined and annealed at 300, 700 and 900 °C for one hour. The ESI (Fig. S7–S10 and Tables S2–S5)† gives the spectra for other ratios under the same conditions. The Mössbauer spectra for sample CaFe1:2 were fitted to two sextets related to α-Fe_2O_3 and α-FeOOH and two duplets related to Fe^{3+} in unidentified sites (Fig. 6). For the CaFe1:2-300 sample, two

Table 1 Crystallite size calculated for the Fe_2O_3, $Ca_2Fe_2O_5$ and $CaFe_2O_4$ phases according to the Scherrer equation for samples in the proportions Ca : Fe 1 : 1, 1 : 2, 1 : 3 and 2 : 1 calcined at 700 and 900 °C for one hour

	Phase and grain size (nm)		
Sample	Fe_2O_3	$Ca_2Fe_2O_5$	$CaFe_2O_4$
$CaFe_2$:1-700	42	17	—
$CaFe_2$:1-900	—	24	42
CaFe1:1-700	47	31	—
CaFe1:1-900	109	42	69
CaFe1:2-700	31	40	—
CaFe1:2-900	65	36	49
CaFe1:3-700	27	40	—
CaFe1:3-900	91	42	52

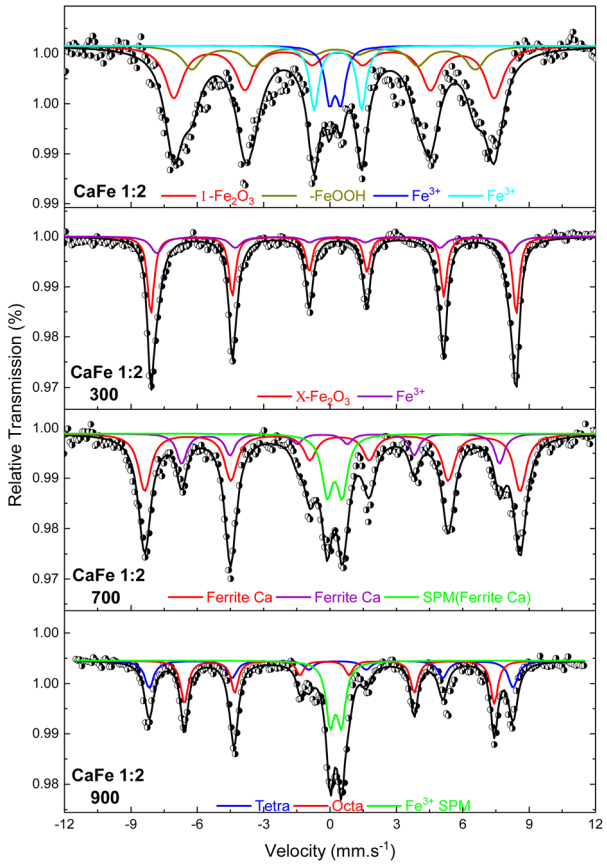

Fig. 6 Mössbauer spectra at room temperature of the samples in the proportion Ca : Fe 1 : 2 calcined at different temperatures of 300, 700 and 900 °C for one hour.

sextets were fitted to α-Fe_2O_3 and γ-Fe_2O_3. For samples CaFe1:2-700 and CaFe1:2-900, two sextets are fitted to octahedral (octa) and tetrahedral (tetra) sites of calcium ferrites and a central duplet referring to Fe^{3+} SPM (superparamagnetic). Fig. 7 shows the sample's relative areas (%) in different Ca : Fe molar ratios (1 : 1, 1 : 2, 1 : 3, 2 : 1) and annealed at 700 and 900 °C for one hour. There is a significant change in the relative areas for Fe^{3+} (tetra + octa) of calcium ferrite. After calcination at 900 °C, the relative area concerning calcium ferrite Fe^{3+} decreases compared to the annealing at 700 °C. The sample CaFe1:2-700 shows this process with 92% of Fe^{3+} from calcium ferrite (Fe^{3+} – octa 64%, Fe^{3+} – tetra 28%) and CaFe1:2-900 decreasing to 70% (Fe^{3+} – octa 32%, Fe^{3+} – tetra 38%). The other groups show similar behavior, sample CaFe2:1-700 (81% Fe^{3+} calcium ferrite) decreasing to CaFe2:1-900 (70% Fe^{3+} – calcium ferrite) and CaFe1:1-700 (73% Fe^{3+} – calcium ferrite) to CaFe1:2-900 (71% Fe^{3+} – calcium ferrite). Sample CaFe1:3-700 shows 96% of Fe^{3+} while CaFe1:3-900 shows 49% of the Fe^{3+} associated with calcium ferrite, as shown in Fig. 7 and tables in the ESI (Tables S2–S5).† Brownmillerite $Ca_2Fe_2O_5$ orthodromic phase contains Fe^{3+} in tetrahedral and octahedral sites,[49–52] while in $CaFe_2O_4$ orthodromic phase, Fe^{3+} cations occupy octahedral sites.[50] The difference between the spectra of the ferrite crystalline phases is not identified in this work due to the analysis at room temperature. Hirabayashi *et al.*[50] analyzed the Mössbauer spectra for different Ca : Fe rations at room temperature and 23 K and could distinguish the two phases found. In Fig. 7, the relative area for the central superparamagnetic duplet (Fe^{3+} – SPM) increases with the annealing temperature, with a maximum value of 51% for CaFe1:3-900, and this behavior has been reported previously.[52] This spectral component may be related to low crystallinity residuals accumulated at the grain boundaries.[52] Relative areas for the goethite (α-FeOOH) are observed only in uncalcined samples due to the thermal decomposition of this phase. The relative areas for α-Fe_2O_3 and γ-Fe_2O_3 are observed for higher iron molar proportions, CaFe1:2-300 (α-Fe_2O_3 – 58%, γ-Fe_2O_3 – 42%) and CaFe1:3-300 (α-Fe_2O_3 – 73%, γ-Fe_2O_3 – 23%). In addition, CaFe1:1-300 and CaFe2:1-300 samples contain 98% and 61% of α-Fe_2O_3, respectively.

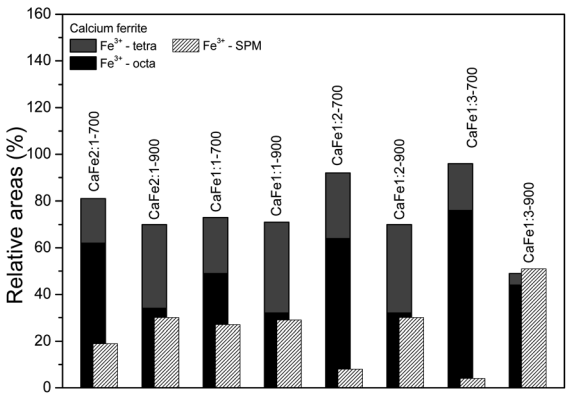

Fig. 7 Relative areas for the iron phases in samples with different Ca : Fe ratios (1 : 1, 1 : 2, 1 : 3 and 2 : 1) calcined at 700 and 900 °C for one hour.

VSM characterization was performed to analyze the magnetic proprieties of the materials CaFe1:2-700 and CaFe1:2-900. No samples showed attraction by a magnet. The hysteresis loops and values of the magnetic properties of calcium ferrites are presented and discussed in ESI S20 and S21.† The samples show low saturation magnetization (Ms), 2.5 emu g^{-1} for CaFe1:2-700 and 1.25 emu g^{-1} for CaFe1:2-900.

Scanning electron microscopy. SEM analyses were performed to scan the morphology and surface of the materials. Fig. 8 shows SEM images for the Ca : Fe 1 : 2 ratio group. CaFe1:2 and CaFe1:2-300 samples show folded sheet surfaces. Circular structures and inserted small particles can be observed on these sheets. This morphology indicates the formation of films of Fe and Ca nitrates and hydroxides during the evaporation of the solutions. Black spots appear when the X-ray hits the material's surface, indicating the precursor's decomposition. After treatment at 700 and 900 °C, the surface of the material changes significantly. A wrinkled surface is formed, and Fig. 8c CaFe1:2-700 and Fig. 8d CaFe1:2-900 show furrows-like microcavities. CaFe1:2-700 shows structures like sharp and bladed petals, like the mineral desert rose with a rough surface Fig. 9. Fig. 9 shows an SEM image at 200 00× magnification with a histogram of petals with a 0.5 to 0.6 μm length range. For CaFe1:2-900, this morphology cannot be

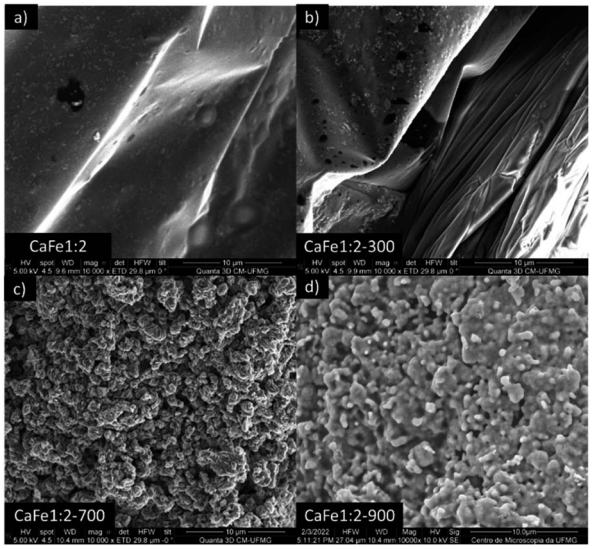

Fig. 8 Adsorbent materials (a) CaFe1:2, (b) CaFe1:2-300, (c) CaFe1:2-700 and (d) CaFe1:2-900 subjected to morphological analysis at 100 00× magnification.

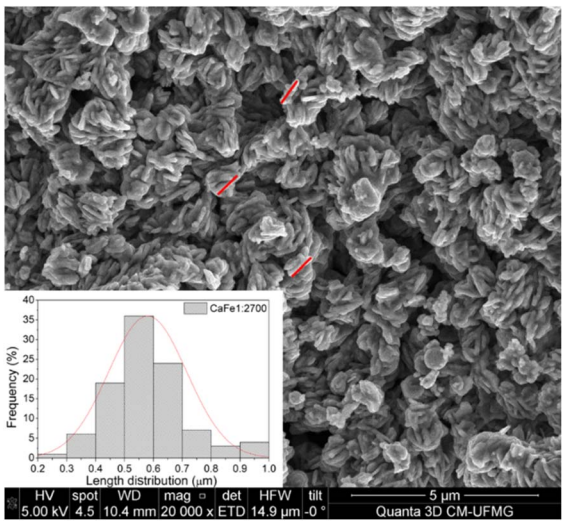

Fig. 9 Sample CaFe1:2-700 at 200 00× magnification with histogram for the length, measured by red lines, of observed overlapping sheetlike structures.

observed; the high-temperature treatment may promote the sintering of the material, and the petals coalesce. The samples CaFe1:2-700 and CaFe1:2-900 were analyzed by N_2 adsorption–desorption, and the surface area was determined by the BET method. Isotherm curves are presented in ESI S19.† The samples CaFe1:2-700 show a surface area equal to 82 $m^2\ g^{-1}$ while CaFe1:2-900 42 $m^2\ g^{-1}$. This result indicates that surface area reduces when the material is annealed at 900 °C for one hour. The CaFe1:1-700, CaFe1:3-700 and CaFe2:1-700 samples seem to have a rougher texture than the CaFe1:1-900, CaFe1:3-900, CaFe2:1-900, which seems to have a flat surface after calcination process because of sintering as shown in the ESI (S15).†

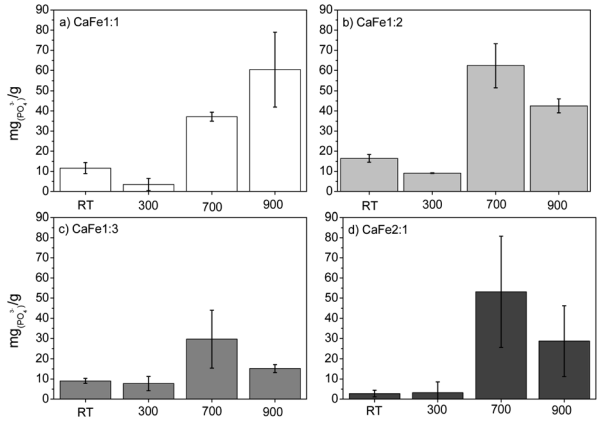

Fig. 10 Preliminary test results of phosphate adsorption (100 mg L^{-1}) after washing samples with water (a) Ca:Fe1:1, (b) Ca:Fe1:2, (c) Ca:Fe1:3 and (d) CaFe2:1 uncalcined (RT) and calcined at 300, 700 and 900 °C for one hour.

Adsorption experiments

Phosphate removal capacity. The adsorption capacity was determined in a bath experiment to select the better adsorbent materials. Phosphate adsorption tests for all annealed samples indicated the presence of significant Ca^{2+} and Fe^{3+}, leading to phosphate removal by precipitation. The ESI (S22–S25)† describes these tests in detail. Therefore, the adsorption tests were performed after extensive washing of the samples to remove any possible Ca^{2+} and Fe^{3+} soluble species. Washed samples uncalcined and calcined at 300 °C for one hour show an adsorption capacity range of 8–16 mg g^{-1} (Fig. 10). Hematite identified by XRD and Mössbauer was detected after 300 °C treatment.

This phase is predominant in these samples, as shown by XRD and Mössbauer (Fig. 3 and 7), which may explain the lower PO_4^{3-} removal capacity. Several works show that hematite, goethite, and other iron oxides can be used as phosphate adsorbents. Ajmal *et al.* (2018)[10] used ferrihydrite, goethite, and magnetite as phosphate adsorbents with good results, 22 mg g^{-1}, 19 mg g^{-1}, and 17 mg g^{-1}, respectively. de Sousa *et al.* (2012)[53] applied hematite to phosphate removal in water with results close to 12 mg g^{-1}. In this work, preliminary phosphate removal test results for iron nitrate uncalcined (Fe) and calcined at 700 (Fe-700) and 900 (Fe-900) present adsorption capacity near 5, 14 and 13 mg g^{-1}, related to hematite phosphate removal ability. The results are present in the ESI (S23).†

The Ca : Fe samples calcined at 700 and 900 °C show better results for phosphate adsorption. After washing, the adsorption capacity decreased significantly for all Ca : Fe ratios, confirming that solubilized Ca^{2+} and Fe^{3+} contribute to phosphate removal. The Ca : Fe 1 : 1 and 1 : 2 ratio groups show better results for phosphate adsorption. In the group with a Ca : Fe ratio 1 : 1, the adsorption capacities of the samples CaFe1:1-700 and CaFe1:1-900 were 37 mg g^{-1} and 60 mg g^{-1}, respectively. The $Ca_2Fe_2O_5$ phase observed by XRD may form due to the 1 : 1 Ca : Fe ratio. The CaFe1:1-900 sample has better crystallinity with sharper

peaks in XRD (see ESI†). By Mössbauer spectroscopy, the samples CaFe1:1-700 and CaFe1:1-900 have similar Fe^{3+}(ferrite) phases (49% – octa and 24% – tetra; 32% – octa and 39% – tetra, respectively). The better crystallinity and less variation in Fe^{3+}(ferrite) phases may enhance their adsorption capacity by forming inner-sphere complexes with phosphate. The presence and availability of Ca^{2+} in the structure may also affect adsorption. The 1 : 1 Ca : Fe ratio may increase the Fe and Ca adsorptive sites in the $Ca_2Fe_2O_5$ and $CaFe_2O_4$ phases. These factors may explain the increased adsorption for these samples.

For the group with a Ca : Fe ratio 1 : 2, the adsorption capacities of the samples CaFe1:2-700 and CaFe1:2-900 were 63 mg g^{-1} and 43 mg g^{-1}, respectively. The adsorption capacity is reduced with the heat treatment at 900 °C for one hour. Calcium ferrites have been identified in this material and coincide with the increase in adsorption capacity compared to CaFe1:2 and CaFe1:2-300. The sample CaFe1:2-900 has better crystallinity with sharper peaks in XRD (Fig. 3); however, the adsorption capacity is reduced. The samples show a change in the relative areas for Fe^{3+} from ferrite, CaFe1:2-700 (Fe^{3+} – octa 64%, Fe^{3+} – tetra 28%) and CaFe1:2-900 (Fe^{3+} – octa 32%, Fe^{3+} – tetra 38%). This modification can make the Fe^{3+} and Ca^{2+} adsorptive sites less available for phosphate interaction and reduce the phosphate removal capacity. Another variable that can influence the adsorption capacity is the surface area. SEM analyses show a loss of roughness, as discussed in Fig. 8. BET analyses can confirm this process, CaFe1:2-700 82 m^2 g^{-1} while CaFe1:2-900 42 m^2 g^{-1}, ESI (S19).† The loss of surface area can lead to a decrease in active adsorption sites, which reduces the adsorption capacity of the CaFe1:2-900 sample. Therefore, the sintering process may decrease adsorption capacity from CaFe1:2-700 to CaFe1:2-900. Iron-based materials, with surface areas more significant than those in this work, showed adsorption capacities close to those of the synthesized materials but with a 5 g L^{-1} adsorbate dosage.[10] They indicate that the $CaFe_2O_4$ and $Ca_2Fe_2O_5$ phases can contribute to the adsorption. Similar behavior occurs in the Ca : Fe 1 : 3 group, CaFe1:3-700 30 mg g^{-1} decreasing to 15 mg g^{-1} for CaFe1:3-900. The lower adsorption capacity for this series may be related to a lower calcium-to-iron ratio, preferably forming hematite. The CaFe2:1 group shows a good adsorption capacity, CaFe2:1-700 53 mg g^{-1} and CaFe2:1-900 29 mg g^{-1}. These results indicate no increase in adsorption capacity, even with a more significant Ca : Fe ratio. Based on the preliminary data, CaFe1:2-700 and CaFe1:2-900 were selected for pH and pH_{PZC} test conditions, competition, isotherm, kinetics (ESI†) and desorption.

pH experiments and pH_{PZC}. The pH can directly influence the surface charge and the species distributions in the medium. Thus, the adsorption conditions can be modified. The pH experiments were performed to understand how pH can change the adsorption capacity. The pH_{PZC} experiments were performed to understand how the environment pH changes the surface charge of the materials.

As observed in Fig. 11, the CaFe1:2-700 sample shows a higher adsorption capacity than CaFe1:2-900 in all pH conditions. Fig. 11 shows that lower pH conditions support better phosphate removal for both samples. At pH 7, the best result for phosphate removal was found for the CaFe1:2-700 sample (66.3 mg g^{-1}). While at pH 5, lower phosphate removal capacity is observed, with the best result being found for CaFe1:2-900 (28.1 mg g^{-1}). The materials decrease the phosphate adsorption capacity at pH > 9. In addition, the pH affects the distribution of phosphate species. At higher pH, the deprotonation of $H_2PO_4^-$ > HPO_4^{2-} and HPO_4^{2-} > PO_4^{3-} results in the presence of more negatively charged species,[1,54] which leads to an electronic repulsion between the adsorbate and the surface of the material. The pH_{PZC} studied the influence of pH on the material surface charge. Fig. 12 presents the data obtained through the experiment and the calculated pH_{PZC} values for samples CaFe1:2-700 7.5 and CaFe1:2-900 7.4. A medium pH lower than pH_{PZC} indicates a predominance of positive surface charges on the material surface, while a medium pH value higher than pH_{PZC} indicates a higher concentration of negative charges on the material surface. According to Fig. 12, at pH values ≥9, negative charges are predominately present on the material texture, leading to repulsion between the adsorbent and the adsorbate. More negative phosphate species (PO_4^{3-}, HPO_4^{2-}) at high pH may decrease the material's phosphate

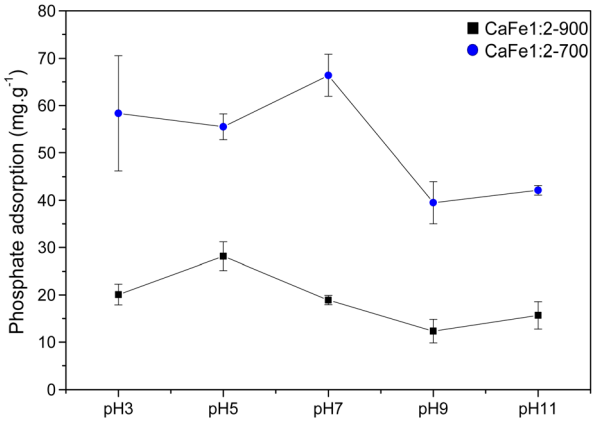

Fig. 11 Phosphate adsorption (100 mg L^{-1}) capacity for CaFe1:2-700 and CaFe1:2-900 samples at different pH.

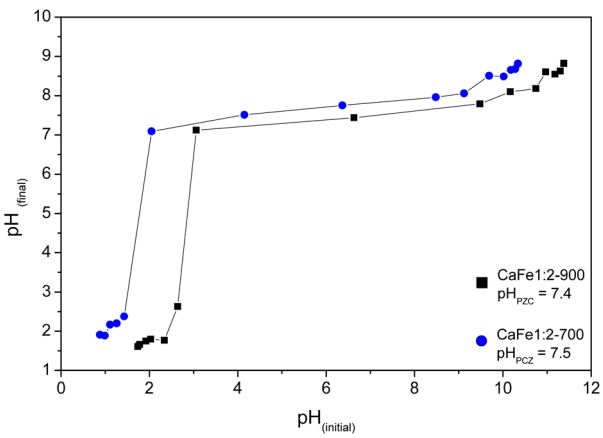

Fig. 12 pH_{PZC} calculated to CaFe1:2-700 and CaFe1:2-900 samples.

adsorption capacity, as observed in the results obtained at different pH. In addition, other works have reported that phosphate ions can compete with hydroxyl ions in iron-based materials. These conditions may be another critical factor in elucidating the phosphate adsorption mechanism in composite materials.[12,54]

Adsorption selectivity – effect of coexisting anions. The effect of coexisting anions was performed to analyze the material selectivity for phosphate. Phosphate and competing ions in the solution used were the same concentration, 100 mg L^{-1}. Coexisting ions such as chloride (Cl^-), sulfate (SO_4^{2-}), nitrate (NO_3^-), carbonate (CO_3^{2-}) and bicarbonate (HCO_3^-) are generally present in the wastewater and could interfere with the uptake of phosphate by the adsorbent through competitive adsorption. Fig. 13 shows the effect of coexisting anions for CaFe1:2-700 and CaFe1:2-900. For the CaFe1:2-700 sample, the presence of Cl^-, NO_3^- and SO_4^{2-} ions presents a significant improvement in the adsorption capacity of the material, with an increase of 45%, 57% and 29%, respectively. These results indicate that Cl^-, NO_3^- and SO_4^{2-} do not compete with PO_4^{3-}. The presence of HCO_3^- and CO_3^{2-} ions decreases the adsorption capacity of the material by 68% and 63%, respectively. For the competition test of the CaFe1:2-900 sample, it was observed that the presence of Cl^- and SO_4^{2-} ions did not cause significant changes in the PO_4^{3-} removal rate. The presence of NO_3^- ions leads to a 45% increase in the phosphate adsorption capacity for the sample. On the other hand, the presence of CO_3^{2-} and HCO_3^- ions leads to a reduction in the phosphate adsorption capacity, reaching only 29% for CO_3^{2-} and 41% for HCO_3^-. Phosphate adsorption on oxide materials may depend on specific sorption.[4] Other anions in solutions, such as Cl^-, NO_3^- and SO_4^{2-}, can affect the ionic strength and undergo nonspecific sorption.[55–58] For the CaFe1:2-900 sample, the presence of Cl^- and SO_4^{2-} did not compete with phosphate for adsorption sites. For the CaFe1:2-700 sample, the presence of Cl^-, NO_3^- and SO_4^{2-} increased the adsorption capacity by enhancing the ionic strength. The phosphate adsorption mechanisms on the material's surface are discussed further in the section. CO_3^{2-} and HCO_3^- ions can be related to changes in the reaction medium's acid-base balance by changing the medium's pH, altering the medium's pH since sodium carbonate and sodium bicarbonate are alkaline salts. In the solutions of PO_4^{3-}/CO_3^{2-} and PO_4^{3-}/HCO_3^- mix (100 mg L^{-1}), the pH starts at 7 in the adsorption process. After 24 h, the pH finished between 8 and 9. As shown in the previous section, the increase in pH causes a decrease in the adsorption capacity of materials due to the presence of hydroxyl ions (OH^-). This factor can explain the observed results since phosphate ions can compete with hydroxyl ions, and the surface charge of the material can reach negative values with increasing pH.[12,54,59,60]

Influence of adsorbate dose – isotherm. The adsorption isotherm test was performed on materials CaFe1:2-700 and CaFe1:2-900 to evaluate the maximum adsorption capacity and attempt to understand the adsorption mechanism for the samples. Fig. 14 presents the experimental points and the Redlich–Peterson isotherm in the short-dash lines. Four isotherm models were applied: Langmuir, Freudlich, Temkin and R–P. The results indicate that as the initial concentration of PO_4^{3-} increases, the adsorption rate of the material also increases. In addition, the adsorption curves of the materials show a non-linear correlation. Table S9 in ESI† shows the calculated parameters of the Langmuir, Freudlich, Temkin and R–P models. The Langmuir isotherm allows to calculate the maximum adsorption capacity (q_{max}). For CaFe1:2-700, q_{max} was 78 mg g^{-1} with an adsorption equilibrium concentration (C_e) close to 90 mg L^{-1}. For the sample CaFe1:2-900, the q_{max} is 36 mg g^{-1}, and C_e is near 41 mg L^{-1}. The R–P adsorption model shows better agreement with the data. For sample CaFe1:2-700, the R^2 0.9487 and sample CaFe1:2-900, R^2 0.9621. Redlich–Peterson isotherm model merges the characteristics of the Langmuir and Freundlich models into a single equation.[61,62] Because of that, the R–P isotherm reduces to the Langmuir model when the n parameter is close to one. When adsorbate concentrations are high, the equation approaches the Freudlich model. The R–P model can be applied to express the sorption process when dealing with adsorbate at high concentrations.[61,62] The values of the n parameter to CaFe1:2-700 are equal to 1.189, and the CaFe1:2-900 n parameter equals 1.094, suggesting that the samples have adsorption behavior similar to the Langmuir

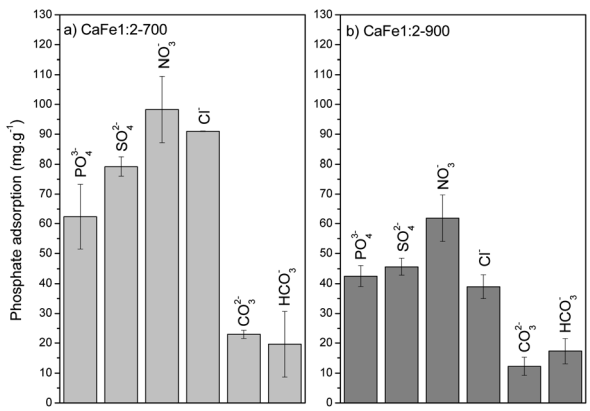

Fig. 13 Competition experiments with different anions (PO_4^{3-}/anion at 100 mg L^{-1}) for (a) CaFe1:2-700 and (b) CaFe1:2-900.

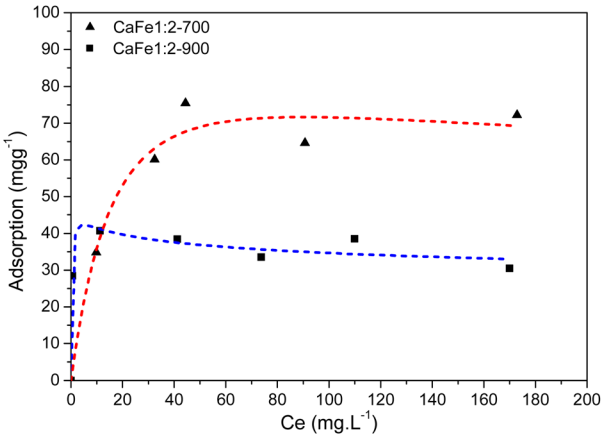

Fig. 14 Phosphate adsorption isotherm for the CaFe1:2-700 and CaFe1:2-900 – Redlich–Peterson isotherm model.

model. Thus, the results suggest that adsorption occurs on a homogeneous surface with adsorption sites with equal adsorption energies, and the adsorption occurs at specific homogeneous sites in a monolayer process to CaFe1:2-700 and CaFe1:2-700. Therefore, observing well-organized structures distributed over the entire material surface by SEM can make the adsorption sites more homogeneous and favor the adsorption according to the formation of a monolayer. Furthermore, the sintering process on the CaFe1:2-900 surface can lead to less homogeneous adsorption domains, favoring the less q_{max} observed.[12,54,59,63]

Phosphate adsorption mechanisms on the material's surface. Adsorption is a process on the surface of the material. The size and shape of adsorption sites, surface area and the chemical species can affect the process. The environment, such as pH and coexisting chemical species, can also change the adsorption capacity. The results show that the annealing temperature can decrease the surface area (*e.g.*, CaFe1:2-700 82 $m^2\ g^{-1}$, CaFe1:2-900 42 $m^2\ g^{-1}$). When the material is prepared at 900 °C, the adsorption sites can be reduced because of the material's sintering, which can reduce the adsorption capacity. However, other variables can also influence the adsorption capacity.

$Ca_2Fe_2O_5$ and $CaFe_2O_4$ phases in the synthesized samples can provide Fe and Ca as adsorption sites on the material's surface, given their strong interaction with phosphate. Fe and Ca can serve as PO_4^{3-} inner-sphere adsorption sites in the samples,[4] as evidenced by their well-distributed presence on the material surfaces in the SEM and EDS spectra provided in ESI S16–S18.† The Fe^{3+} phases present in the ferrite structure could aid in phosphate removal. The $Ca_2Fe_2O_5$ phase is present in both heat treatments (700 and 900 °C). It is noticed that the $CaFe_2O_4$ phase appears preferentially after calcination at 900 °C for one hour. It is known that higher temperatures are required to form the $CaFe_2O_4$ phase. For the formation of the $CaFe_2O_4$ phase, a reconstructive transformation can occur with the entire movement of octahedral sites.[64,65] The change in the relative areas of the tetrahedral and octahedral sites of Fe^{3+}, observed by Mössbauer spectroscopy, can indicate these movements. However, a decrease in Fe^{3+} was noted in calcium ferrite for CaFe1:2-700 and CaFe1:2-900 (from 92% to 70%), CaFe1:3-700 and CaFe1:3-900 (from 96% to 49%), and CaFe2:1-700 and CaFe2:1-900 (from 81% to 70%). This reduction of Fe^{3+} in ferrite phases could potentially diminish the phosphate adsorption capacity of these materials because the Fe^{3+} on the surface of the material is less available.

The calcium in the ferrite surface can also work as an adsorption site for inner-sphere complex formation. Changing the Fe^{3+} positions in the ferrite structure can also cause changes in the Ca^{2+} position. It is possible to see that a higher proportion of Ca concerning Fe does not bring significant benefits for the adsorption of PO_4^{3-}, as in the case of samples CaFe2:1-700 and CaFe2:1-900. Calcination at 900 °C for 1 hour enhanced the crystallinity of the materials, potentially improving adsorption, as observed in CaFe1:1-700 and CaFe1:1-900 samples. The presence of Ca may be beneficial for the adsorption of phosphate since this element has good affinity for the PO_4^{3-} species, but other studies need to be conducted to elucidate the role of Ca in the adsorption of phosphate in the structure of the ferrites $Ca_2Fe_2O_5$ and $CaFe_2O_4$ separately. Therefore, the presence of $Ca_2Fe_2O_5$ and $CaFe_2O_4$ phases is important to improve the adsorption capacity of adsorbent materials.

The environment can influence the adsorption capacity. Loganathan *et al.*[4] demonstrated that the adsorption mechanisms of phosphate to oxides and hydroxides are primarily governed by ion exchange through forming inner-sphere complexes (specific sorption), forming monodentate or bidentate complexes.[55–58,66] This finding aligns with the data obtained from the R–P isotherm model, which indicates homogeneous adsorption sites for PO_4^{3-}. Conversely, Cl^-, NO_3^-, and SO_4^{2-} ions may follow a nonspecific adsorption mechanism, forming outer-sphere complexes on oxides and hydroxides.[67,68] This species can change the ionic strength and may play a role in phosphate adsorption. Anions that form inner-sphere complexes are either slightly affected by ionic strength or adsorb more at higher ionic strength.[55–58] Iron oxides adsorb phosphate following the inner-sphere phosphate complex formation, and the adsorption can increase with increasing electrolyte concentration. This effect is typically ascribed to alterations in the electric potential at the interface. The ionic strength strongly affects the adsorption of anions that form outer-sphere complexes. These anions compete with weakly adsorbed anions like NO_3^-, which bind electrostatically to the surface. These results suggest that phosphate anions bind specifically to calcium ferrite materials by forming inner-sphere complexes with Ca and Fe. The Cl^-, NO_3^- and SO_4^{2-} anions can form outer-sphere complexes and do not compete or compete weakly with inner-sphere adsorption sites or increase the phosphate adsorption capacity by increasing the ionic strength.

The elevated pH (pH > 9) introduces high OH^- concentration, and the phosphate adsorption decreases by 52% for CaFe1:2-700 (39 mg g^{-1}) and 56% for CaFe1:2-900 (12 mg g^{-1}). The OH^- can compete with phosphate for Ca^{2+} and Fe^{2+} adsorptive sites, forming an inner-sphere complex.[23] The coexisting ions, such as HCO_3^- and CO_3^{-2}, also reduce the adsorption, possibly due to the alkaline characteristic of these anions. Therefore, the adsorption process may be related to chemisorption on the surface of the material.

Desorption experiments

The desorption bath experiments were performed to evaluate and elucidate the better environment for phosphate release under different conditions. Fig. 15 shows the results of the desorption study under different conditions. The first condition analyzed was alkaline pH with different NaOH concentrations (0.1, 0.5, and 1.0 mol L^{-1}). The desorption capacity for both samples increased when the NaOH concentration increased. Better results were shown for NaOH (1.0 mol L^{-1}) condition, CaFe1:2-700 with 15.1% (9.4 mg g^{-1}) and CaFe1:2-900 with 38.9% (16.5 mg g^{-1}). This result indicates that the presence of OH^- can improve the PO_4^{3-} desorption. Other works have reported that alkaline conditions can promote PO_4^{3-} desorption for adsorbent regeneration.[10,12] The second condition analyzed was in different ionic strengths (Fig. 15). Then, the experiment was carried out under

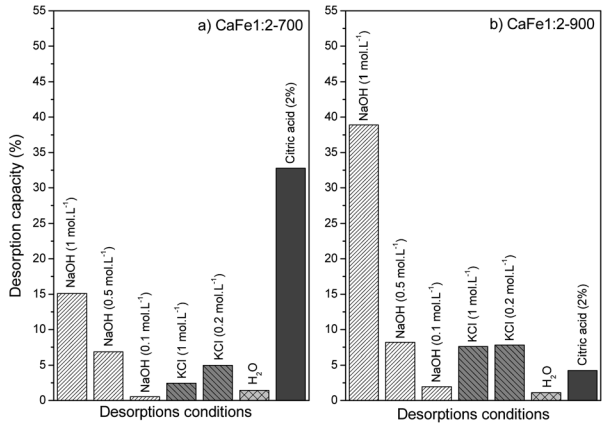

Fig. 15 Desorption capacity for samples (a) CaFe1:2-700 and (b) CaFe1:2-900 in different conditions.

different KCl concentrations (0.2 and 1.0 mol L^{-1}). For the CaFe1:2-700 sample, the desorption capacity was 4.9% (4.9 mg L^{-1}) and 2.4% (2.4 mg L^{-1}) for 0.2 and 1.0 mol L^{-1} conditions. Now, for the CaFe1:2-900 sample, the results did not indicate a difference between the conditions studied, 7.6% (7.8 mg L^{-1}) and 7.8% (7.1 mg L^{-1}) for 0.2 and 1.0 mol L^{-1} KCl concentrations respectively. The more concentrated KCl (1 mol L^{-1}) cannot promote more PO_4^{3-} desorption. With only water, the desorption capacity was the lowest, 1.4% (0.8 mg L^{-1}) and 1.1% (0.4 mg L^{-1}) for CaFe1:2-700 and CaFe1:2-900, respectively. The third condition analyzed followed the experiment described by Ministério da Agricultura, Pecuária e Abastecimento (MAPA). The results show the highest desorption capacity for sample CaFe1:2-700, 32.7% (20.4 mg g^{-1}). For sample CaFe1:2-900, the desorption capacity is around 4% (1.8 mg g^{-1}). However, the supernatant shows a yellow coloring, indicating the leaching of Fe and Ca. The atomic absorption confirms that Fe 9.7 mg L^{-1} and Ca 112.7 mg L^{-1} are available in the supernatant for CaFe1:2-700 and Fe 5.9 mg L^{-1} and Ca 99.9 mg L^{-1} for CaFe1:2-900 after contact with acid citric solution. So, the structure of the ferrites and ferrous minerals may be breaking down in contact with the citric acid solution. As the acidic solution degrades the structure of the material, reapplication is hindered, as indicated by the yellowish coloration of the supernatant after 30 min. Maintaining the formed ferrite phases is important for the material to retain its adsorptive properties. Therefore, using acid solutions in the desorption of phosphate in ferrite-based materials is not beneficial.

Conclusions

In this study, calcium ferrites were synthesized by thermal decomposition and characterized by different techniques. MEV micrographs show the surface change with the thermal treatment; samples calcined at 700 °C showed more roughness than samples calcined at 900 °C, and the BET results confirm this observation. The Mössbauer spectroscopy indicates the calcium ferrites formation after heat treatment at 700 and 900 °C for one hour, and XRD confirms the presence of $CaFe_2O_4$ (PDF 00-032-0168) and $Ca_2Fe_2O_5$ (COD 90-134-69), both in orthorhombic structure. The VSM analyses indicate a soft ferromagnetic material formed but are challenging to apply for the material's recovery for adsorption application in water.

The materials calcined at 700 and 900 °C for one hour showed better adsorption results than those uncalcined or calcined at 300 °C. The preliminary test for phosphate removal indicates that the presence of $Ca(OH)_2$ and CaO affects the adsorption capacity. The material was washed four times with water, the test was repeated, and the removal capacity decreased. After washing, two samples showed better results, CaFe1:2-700 62 mg g^{-1} and CaFe1:2-900 43 mg g^{-1}. High OH^- concentrations reduce the adsorption capacity by 50% on average. Other ions coexisting with PO_4^{3-} in water can increase the adsorption capacity, such as Cl^-, NO_3^- and SO_4^{2-}, while CO_3^{2-} and HCO_3^- decrease the phosphate removal. Alkaline conditions showed better phosphate desorption, CaFe1:2-700 with 15.1% and CaFe1:2-900 with 38.9%. The acidic conditions with 2% citric acid affect the structure of the material. Material reusability is difficult due to the strong bond between sorbent and sorbate. The materials investigated in this study demonstrate satisfactory phosphate removal in water and are a promising sorbent for this pollutant.

The different conditions tested for phosphate desorption can expand, albeit in a simple way at first, the understanding of the complexity of different reapplication media, such as soil, which presents more variables such as pH, cation exchange capacity, organic matter, microorganisms, and weathering, for example. Additionally, materials can be tested in continuous flow desorption to simulate the passage of water or others extracting solution through the material and evaluate phosphate dynamics release. The material can be tested in wastewater for soluble phosphate removal in future work. In addition, a magnetic phase of ferrite ($CaFe_2O_4$ – spinel) can be synthesized to evaluate the phosphate adsorption capacity, phosphate recovery and material reusability.

Author contributions

Matheus H. P. Araújo preparation, creation, and presentation of the published work by those from the original research group, specifically critical review and revision – including pre-or post-publication stages, conducting a research and investigation process, specifically performing the experiments and data collection. José D. Ardisson performed the experiments, data collection, critical review, commentary, and revision. Alisson C. Krohling, performing the experiments, data collection and commentary. Rochel M. Lago critical review, commentary, and revision. Walber G. G. Júnior, conducting a research and investigation process, specifically performing the experiments or data/evidence collection. Juliana C. Tristão oversight and leadership responsibility for the research activity planning and execution, including mentorship external to the core team, critical review, commentary, and revision.

Conflicts of interest

There are no conflicts to declare.

Acknowledgements

The Fundação de Amparo à Pesquisa do Estado de Minas Gerais (FAPEMIG) (project APQ-00770-22) partially supported this study and Coordenação de Aperfeiçoamento de Pessoal de Nível Superior (CAPES) from Brazil for the doctorate scholarship. The Conselho Nacional de Desenvolvimento Científico e Tecnológico (CNPq) partially supported this study (project 406042/2022-5). The Núcleo Multiusuário from UFV – campus Florestal for atomic absorption analyses. The Centro de Microscopia da UFMG for the SEM/EDS images. The Laboratório multiusuários de Difração de raios from UFV – campus Rio Paranaíba for the XRD analyses.

Notes and references

1 H. Bacelo, A. M. A. Pintor, S. C. R. Santos, R. A. R. Boaventura and C. M. S. Botelho, *Chem. Eng. J.*, 2020, **381**, 122566.
2 G. M. Filippelli, *Elements*, 2008, **4**, 89–95.
3 C. Klein and S. A. A. Agne, *Revista Eletrônica em Gestão, Educação e Tecnologia Ambiental*, 2012, 1713–1721.
4 P. Loganathan, S. Vigneswaran, J. Kandasamy and N. S. Bolan, *Crit. Rev. Environ. Sci. Technol.*, 2014, **44**, 847–907.
5 G. Pantano, G. M. Grosseli, A. A. Mozeto and P. S. Fadini, *Quim. Nova*, 2016, **39**, 732–740.
6 F. Peterson and D. Wasley, *Phosphorus: Sources, Forms, Impact on Water Quality-A General Overview*, 2007.
7 J. Shen, L. Yuan, J. Zhang, H. Li, Z. Bai, X. Chen, W. Zhang and F. Zhang, *Plant Physiol.*, 2011, **156**, 997–1005.
8 L. Roshanfekr Rad and M. Anbia, *J. Environ. Chem. Eng.*, 2021, **9**(5), 106088.
9 W. Huang, Y. Zhang and D. Li, *J. Environ. Manage.*, 2017, **193**, 470–482.
10 Z. Ajmal, A. Muhmood, M. Usman, S. Kizito, J. Lu, R. Dong and S. Wu, *J. Colloid Interface Sci.*, 2018, **528**, 145–155.
11 J. Liu, R. Zhu, L. Ma, H. Fu, X. Lin, S. C. Parker and M. Molinari, *Geoderma*, 2021, **383**(1), 114799.
12 W. Gu, Q. Xie, C. Qi, L. Zhao and D. Wu, *Powder Technol.*, 2016, **301**, 723–729.
13 M. Silva and J. Baltrusaitis, *Environ. Sci.*, 2020, **6**, 3178–3194.
14 S. Ahmed, M. N. Ashiq, D. Li, P. Tang, F. Leroux and Y. Feng, *Recent Pat. Nanotechnol.*, 2019, **13**, 3–16.
15 C. Han, J. Lalley, N. Iyanna and M. N. Nadagouda, *Mater. Chem. Phys.*, 2017, **198**, 115–124.
16 Y. Jia, H. Wang, X. Zhao, X. Liu, Y. Wang, Q. Fan and J. Zhou, *Appl. Clay Sci.*, 2016, **129**, 116–121.
17 S. M. Ashekuzzaman and J. Q. Jiang, *Chem. Eng. J.*, 2014, **246**, 97–105.
18 K. Yang, L. G. Yan, Y. M. Yang, S. J. Yu, R. R. Shan, H. Q. Yu, B. C. Zhu and B. Du, *Sep. Purif. Technol.*, 2014, **124**, 36–42.
19 P. Cheng, D. Chen, H. Liu, X. Zou, Z. Wu, J. Xie, C. Qing, D. Kong and T. Chen, *J. Mol. Liq.*, 2018, **254**, 145–153.
20 A. Sonoda, Y. Makita, Y. Sugiura, A. Ogata, C. Suh, J. hoon Lee and K. Ooi, *Sep. Purif. Technol.*, 2020, **249**(15), 117143.
21 K. A. Tee, S. Ahmed, M. A. H. Badsha, K. C. J. Wong and I. M. C. Lo, *Clean Technol. Environ. Policy*, 2023, **25**, 1783–1805.
22 A. Nuryadin and T. Imai, in *IOP Conference Series: Earth and Environmental Science*, IOP Publishing Ltd, 2021, vol. 926.
23 W. Gu, Q. Xie, C. Qi, L. Zhao and D. Wu, *Powder Technol.*, 2016, **301**, 723–729.
24 P. S. Kumar, L. Korving, M. C. M. van Loosdrecht and G. J. Witkamp, *Water Res.: X*, 2019, **4**, 100029.
25 Y. Wei, K. Guo, H. Wu, P. Yuan, D. Liu, P. Du, P. Chen, L. Wei and W. Chen, *Chem. Commun.*, 2021, **57**, 1639–1642.
26 N. Doebelin and R. Kleeberg, *J. Appl. Crystallogr.*, 2015, **48**, 1573–1580.
27 F. B. A. de Freitas, M. Y. d. F. Câmara and D. F. M. Freitas, Determinação do PCZ de adsorventes naturais utilizados na remoção de contaminantes em soluções aquosas., *Blucher Chemistry Proceedings 5o Encontro Regional de Química & 4o Encontro Nacional de Química*, 2015, vol. 3.
28 D. K. Smith, *Acta Crystallogr.*, 1962, **15**, 1146–1152.
29 S. Damerio, P. Nukala, J. Juraszek, P. Reith, H. Hilgenkamp and B. Noheda, *npj Quantum Mater.*, 2020, **5**, 33.
30 B. F. Decker and J. S. Kasper, *Acta Crystallogr.*, 1957, **10**, 332–337.
31 P. Giannozzi, S. Baroni, N. Bonini, M. Calandra, R. Car, C. Cavazzoni, D. Ceresoli, G. L. Chiarotti, M. Cococcioni, I. Dabo, A. Dal Corso, S. De Gironcoli, S. Fabris, G. Fratesi, R. Gebauer, U. Gerstmann, C. Gougoussis, A. Kokalj, M. Lazzeri, L. Martin-Samos, N. Marzari, F. Mauri, R. Mazzarello, S. Paolini, A. Pasquarello, L. Paulatto, C. Sbraccia, S. Scandolo, G. Sclauzero, A. P. Seitsonen, A. Smogunov, P. Umari and R. M. Wentzcovitch, *J. Phys.: Condens.Matter*, 2009, **21**, 395502.
32 B. Hammer, L. B. Hansen and J. K. Nørskov, *Phys. Rev. B: Condens. Matter Mater. Phys.*, 1999, **59**, 7413–7421.
33 P. E. Blöchl, *Phys. Rev. B: Condens. Matter Mater. Phys.*, 1994, **50**, 17953–17979.
34 I. Kagomiya, Y. Hirota, K. I. Kakimoto, K. Fujii, M. Shiraiwa, M. Yashima, A. Fuwa and S. Nakamura, *Phys. Chem. Chem. Phys.*, 2017, **19**, 31194–31201.
35 S. Damerio, A. A. Kaverzin, V. Ocelík, G. R. Hoogeboom, B. J. van Wees and B. Noheda, *Adv. Electron. Mater.*, 2022, **8**, 2100963.
36 S. Dudarev and G. Botton, *Phys. Rev. B: Condens. Matter Mater. Phys.*, 1998, **57**, 1505–1509.
37 V. I. Anisimov, J. Zaanen and O. K. Andersen, *Phys. Rev. B: Condens. Matter Mater. Phys.*, 1991, **44**, 943–954.
38 V. I. Anisimov, A. I. Poteryaev, M. A. Korotin, A. O. Anokhin and G. Kotliar, *J. Phys.: Condens. Matter*, 1997, **9**, 7359–7367.
39 I. Timrov, N. Marzari and M. Cococcioni, *Phys. Rev. B*, 2018, **98**, 085127.
40 N. Varini, D. Ceresoli, L. Martin-Samos, I. Girotto and C. Cavazzoni, *Comput. Phys. Commun.*, 2013, **184**, 1827–1833.
41 C. F. Matta and R. J. Boyd, *The Quantum Theory of Atoms in Molecules*, Wiley, 2007.
42 A. M. Pendás, A. Costales and V. Luaña, *J. Phys. Chem. B*, 2002, **102**, 6937–6948.
43 A. Otero-de-la-Roza, E. R. Johnson and V. Luaña, *Comput. Phys. Commun.*, 2014, **185**, 1007–1018.
44 W. Brockner, C. Ehrhardt and M. Gjikaj, *Thermochim. Acta*, 2007, **456**, 64–68.

45 K. Deshpande, A. Mukasyan and A. Varma, *Chem. Mater.*, 2004, **16**, 4896–4904.
46 V. Berbenni, A. Marini, G. Bruni and C. Milanese, *J. Anal. Appl. Pyrolysis*, 2008, **82**, 255–259.
47 A. Vedrtnam, K. Kalauni, S. Dubey and A. Kumar, *AIMS Mater. Sci.*, 2020, **7**, 800–835.
48 M. Kumar, H. Singh Dosanjh, S. Sonika, J. Singh, K. Monir and H. Singh, *Environ. Sci.*, 2020, **6**, 491–514.
49 T. Hidayat, D. Shishin, S. A. Decterov and E. Jak, *Metall. Mater. Trans. B*, 2016, **47**, 256–281.
50 D. Hirabayashi, Y. Sakai, T. Yoshikawa, K. Mochizuki, Y. Kojima, K. Suzuki, K. Ohshita and Y. Watanabe, *Hyperfine Interact.*, 2006, **167**, 809–813.
51 A. Bloesser, J. Timm, H. Kurz, W. Milius, S. Hayama, J. Breu, B. Weber and R. Marschall, *Sol. RRL*, 2020, 1–7.
52 B. F. Amorim, M. A. Morales, F. Bohn, A. S. Carriço, S. N. De Medeiros and A. L. Dantas, *Phys. B*, 2016, **488**, 43–48.
53 A. F. de Sousa, T. P. Braga, E. C. C. Gomes, A. Valentini and E. Longhinotti, *Chem. Eng. J.*, 2012, **210**, 143–149.
54 D. A. Almasri, N. B. Saleh, M. A. Atieh, G. McKay and S. Ahzi, *Sci. Rep.*, 2019, **9**, 3232.
55 J. Antelo, M. Avena, S. Fiol, R. López and F. Arce, *J. Colloid Interface Sci.*, 2005, **285**, 476–486.
56 G. Li, S. Gao, G. Zhang and X. Zhang, *Chem. Eng. J.*, 2014, **235**, 124–131.
57 J. C. Ryden, J. R. McLaughlin and J. K. Syers, *J. Soil Sci.*, 1977, **28**(1), 72–92.
58 G. Zhang, H. Liu, R. Liu and J. Qu, *J. Colloid Interface Sci.*, 2009, **335**, 168–174.
59 G. Zhang, H. Liu, R. Liu and J. Qu, *J. Colloid Interface Sci.*, 2009, **335**, 168–174.
60 R. Chitrakar, S. Tezuka, A. Sonoda, K. Sakane, K. Ooi and T. Hirotsu, *J. Colloid Interface Sci.*, 2006, **298**, 602–608.
61 F. Brouers and T. J. Al-Musawi, *J. Mol. Liq.*, 2015, **212**, 46–51.
62 K. Y. Foo and B. H. Hameed, *Chem. Eng. J.*, 2010, **156**, 2–10.
63 J. Wang and X. Guo, *Chemosphere*, 2020, **258**, 1–25.
64 Á. M. Arévalo-López, A. J. Dos Santos-García, E. Castillo-Martínez, A. Durán and M. Á. Alario-Franco, *Inorg. Chem.*, 2010, **49**, 2827–2833.
65 E. E. Ateia, G. Abdelatif and F. S. Soliman, *J. Mater. Sci.: Mater. Electron.*, 2017, **28**, 5846–5851.
66 L. Hou, Q. Liang and F. Wang, *RSC Adv.*, 2020, **10**, 2378–2388.
67 Q. Yang, X. Wang, W. Luo, J. Sun, Q. Xu, F. Chen, J. Zhao, S. Wang, F. Yao, D. Wang, X. Li and G. Zeng, *Bioresour. Technol.*, 2018, **247**, 537–544.
68 N. Y. Acelas and E. Flórez, *Adsorption*, 2018, **24**, 243–248.